UC Irvine
UC Irvine Electronic Theses and Dissertations

Title
Parametric Resonance of Magnetization Excited by Electric Field

Permalink
https://escholarship.org/uc/item/81p4091n

Author
Chen, Yu-Jin

Publication Date
2016

Peer reviewed|Thesis/dissertation

UNIVERSITY OF CALIFORNIA,
IRVINE

Parametric Resonance of Magnetization
Excited by Electric Field

THESIS

submitted in partial satisfaction of the requirements
for the degree of

MASTER OF SCIENCE

in Chemical and Material Physics

by

Yu-Jin Chen

Thesis Committee:
Professor Ilya N. Krivorotov, Chair
Professor Suzanna Siwy
Professor Ruqian Wu

2016

TABLE OF CONTENTS

LIST OF FIGURES

ACKNOWLEDGMENTS

I would first like to thank my advisor, Ilya Krivorotov, who has given me the great opportunity to study and solve interesting physics problems in his group. He has been patient and supportive through my research and has made the frustrations of setbacks much easier to deal with through his pragmatic personality. Our group is also one that emulates this supportive behavior, and it is an environment that has been a pleasure to work in. Most of all, I must thank him for teaching me how to be a good scientist by his example.

Next, I would like to thank my coworker who worked most closely with me on this project, Han Kyu Lee. He has been a great labmate and friend, who spent many late hours with me discussing this project and making so many of the measurements. I would also like to thank Igor Barsukov, who spent much of his scant free time helping us on this project.

I would also like to thank our theory collaborators Roman Verba, Vasil Tiberkevich, and Andrei Slavin for developing the theory we used to analyze our data and helping to guide the project while it was under way.

My thanks also go to my labmates, past and present, in the Krivorotov Group who have contributed to a positive and cooperative environment. I would especially like to thank Graham Rowlands, who got me started on microwave measurements and understanding magnetic dynamics. He also inspired me to return to my interest in programming and using that knowledge to improve my research.

Finally, I cannot adequately express the gratitude I have for my family and friends who have supported me in my research.

ABSTRACT OF THE THESIS

Parametric Resonance of Magnetization

Excited by Electric Field

By

Yu-Jin Chen

Master of Science in Chemical and Material Physics

University of California, Irvine, 2016

Professor Ilya N. Krivorotov, Chair

This thesis describes the experiments that demonstrate the ability to efficiently excite magnetization parametrically by electric field. The experiments are done with nanoscale magnetic tunnel junctions, which are multilayer thin film devices patterned into nanopillar shape. One of the layers possesses strong perpendicular magnetic anisotropy and exhibits strong voltage-controlled magnetic anisotropy. This magneto-electric effect allows one to modulate the perpendicular magnetic anisotropy of the layer and parametrically excite large-amplitude oscillations of the magnetization. The results of this experiment show that it is possible to parametrically excite resonance in a magnetic nanostructure using electric field and that the threshold voltage for this process is low: it is found to be well below 1 Volt. This paves the way towards developing energy-efficient spintronic devices based on parametric excitation of magnetization by electric field.

Chapter 1

Introduction

Manipulation of magnetization by electric field is a central goal of spintronics. Recent progress towards this goal includes magnetization reversal [12, 13] and ferromagnetic resonance [14, 15] driven by electric field. In particular, the effect known as voltage-controlled magnetic anisotropy is featured as the magneto-electric mechanism for controlling magnetization by electric field. This thesis will describe the experiment that demonstrates how this magneto-electric effect can efficiently manipulate magnetization by electric field through parametric excitation. The results of this experiment further the development of spintronic devices for technologically relevant applications, such as spin wave logic devices. [35]

In Chapter 2, I will give background information that is necessary for understanding the physics in the experiments. It will include an overview of several significant effects in the nanostructures called magnetic tunnel junctions that are used in the experiment. It will also describe the physics of some experimental methods used in characterizing the samples.

In Chapter 3, I describe the experiment which demonstrates the ability to excite parametric resonance of magnetization in a nanodevice via electric field. It describes the experimental

methods, including specific sample configuration, some details of the preparation of the setup, and the results which are compared to theory.

Finally, I present conclusions and future outlook in Chapter 4.

Chapter 2

Background

2.1 Magnetic Tunnel Junctions

The devices under study are nanoscale magnetic tunnel junctions (MTJs), which in their most basic form are trilayer structures with two ferromagnetic layers separated by an insulating layer. As depicted in FIg. 2.1, typical thicknesses of the layers range from a few nanometers down to less than one nanometer. Typically, MTJs are patterned into a nanopillar structures with lateral dimensions that range from sub-micron down to tens of nanometers.

One useful property of MTJs is the tunneling magnetoresistance (TMR) effect, with which we can electrically read out the relative orientation of the ferromagnetic layers by measuring the resistance of the MTJ. The tunneling magnetoresistance value then describes the difference in resistance between the parallel (low resistance) and anti-parallel (high resistance) orientations of the two magnetizations.

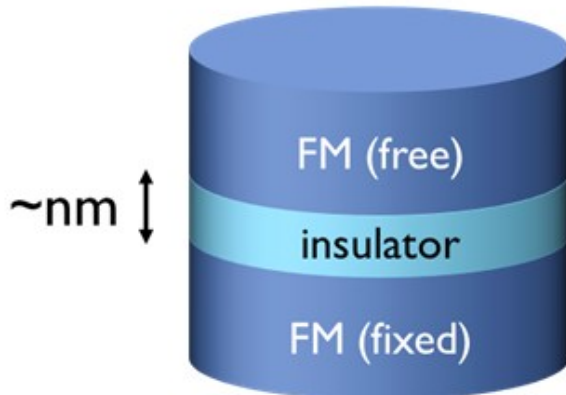$$TMR = \frac{R_{AP} - R_P}{R_P} \tag{2.1}$$

Figure 2.1: **Magnetic tunnel junction.** Schematic of a magnetic tunnel junction, a nanoscale trilayer structure with two ferromagnets separated by an insulating spacer.

The TMR model developed by Julliere [10]) is schematically illustrated in Fig. 2.2 and is valid for amorphous barriers. The origin of the effect is attributed to spin-dependent tunneling through the MTJ's insulating barrier when voltage is applied perpendicular to the plane of the MTJ layers (CPP or current-perpendicular-to-plane geometry). The electrons must tunnel through the insulating barrier, and the tunneling conductance of the MTJ depends on the density of states for majority and minority bands of both ferromagnets:

$$G \propto D_{\uparrow,1} D_{\uparrow,2} + D_{\downarrow,1} D_{\downarrow,2} \tag{2.2}$$

$$G_p \propto D_1^{maj} D_2^{maj} + D_1^{min} D_2^{min} \tag{2.3}$$

$$G_{Ap} \propto D_1^{maj} D_2^{min} + D_1^{min} D_2^{maj}. \tag{2.4}$$

Here G_P and G_{AP} are the conductances for the parallel and anti-parallel magnetization configurations, respectively. The $D_\uparrow$ and $D_\downarrow$ are the density of states for up and down spins, respectively, and the superscripts maj and min denote majority and minority bands, respectively. The numbers 1 and 2 denote the corresponding ferromagnet. As shown in Fig. 2.2 and equations (2.3) and (2.4), the current is essentially split into two currents. The majority band dominates in the parallel case and ends up being the high conductance (low

resistance) state while the anti-parallel case results in low conductance for both channels (high resistance).
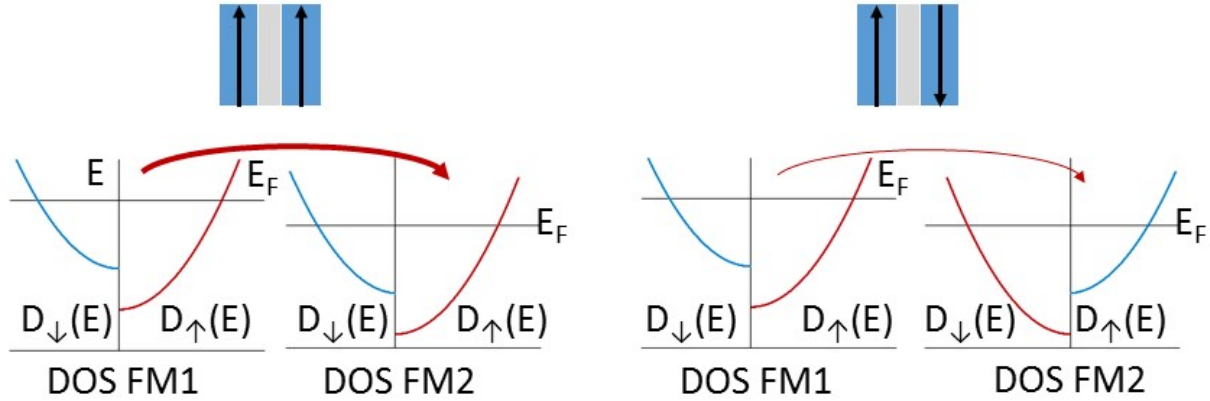

Figure 2.2: **Tunneling magnetoresistance schematic.** Basic schematic of tunneling magnetoresistance through an amorphous barrier. The different orientations of magnetization lead to different density of states and therefore different tunneling conductance.

Tunneling through crystalline MgO barriers is more complex but also results in different resistance states depending on relative orientation of the magnetizations. The conductance is strongly dependent on the density of states of the Bloch states. In particular, it is strongly dependent on the symmetry of the Bloch states in the ferromagnets as well as the evanescent states in the insulator. These, in turn, depend on the relative orientation of the magnetizations of the ferromagnets. [9]

The TMR effect by itself does not help to study magnetization dynamics if both layers in the MTJ are free to move and thus obscure the finer details of the behavior of a single ferromagnet. To compensate for this, there are several ways to effectively pin one of the layers against easy manipulation by magnetic field. One way is to simply make one of the layers thicker, thereby requiring more energy to rotate the magnetization. Another way is to place an antiferromagnet adjacent to one of the layers. This couples the ferromagnetic layer to the antiferromagnet by exchange bias [6] and can leave the ferromagnet strongly pinned.

In our structures, both methods are used to pin one of the ferromagnetic layers (called the fixed layer), and the layer that is relatively easy to manipulate is called the free layer.
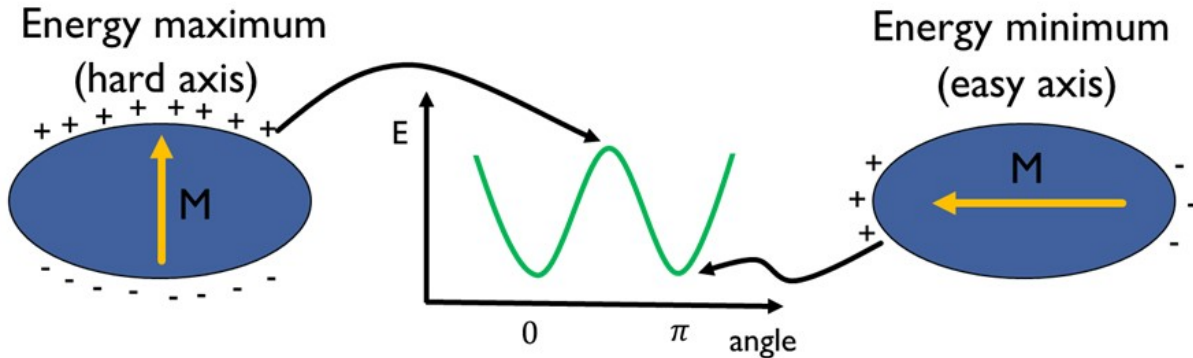

Figure 2.3: **Shape anisotropy.** Shape anisotropy creates stable states for the free layer magnetization. In the case of uniaxial anisotropy, the magnetization prefers to lie along an easy axis (parallel or anti-parallel).

Typically, the MTJs we study are patterned into nanopillar structures, and the lateral cross section can be a non-circular shape. Often, as in this thesis, we use samples that have elliptical cross section, as shown in Fig. 2.3. This gives rise to an in-plane shape anisotropy (a preferred direction for magnetization) that also helps to define the parallel and anti-parallel orientations of the magnetization. The shape anisotropy is due to the demagnetization energy, which arises from buildup of magnetic charge at the boundaries of a sample due to the shape of the sample. [6] In the case of a uniaxial anisotropy, the magnetization lies along a preferred easy-axis (or along a preferred easy-plane). In particular, the parallel and anti-parallel alignments of the free and fixed layers are usually along the easy-axis of the sample.

In order to read orientations of magnetizations other than parallel or anti-parallel, the resistance of the structure must be determined for intermediate angles. The angular dependence

of the *conductance* is modelled as:

$$G(\theta) = \langle G \rangle (1 + P_1 P_2 \cos(\theta)) \tag{2.5}$$

where $\langle G \rangle = (G_P + G_{AP})/2$ is the average of the parallel and anti-parallel state conductances, P_1 and P_2 are the spin polarizations of each ferromagnet, and the angle θ is the angle between the magnetizations of the two layers. [1] This makes the conductance proportional to the projection of the free layer magnetization along the direction of the fixed layer.

2.2 Magnetization Dynamics

Magnetization dynamics for a single spin (or macrospin) is often instructive when trying to understand the dynamics of the free layer in a magnetic nanostructure. The macrospin magnetization dynamics can be described by the Landau-Lifshitz-Gilbert (LLG) equation, which has the form:

$$\frac{d\mathbf{M}}{dt} = -\gamma \mathbf{M} \times \mathbf{H}_{\text{eff}} + \frac{\alpha}{M_s} \mathbf{M} \times \frac{d\mathbf{M}}{dt} \tag{2.6}$$

where $\mathbf{M}$ is the magnetization (with M_s as the saturation magnetization), γ is the gyromagnetic ratio, $\mathbf{H}_{\text{eff}}$ is the effective field, and α is the Gilbert damping. The effective field $\mathbf{H}_{\text{eff}}$ is the gradient of the free energy with respect to the magnetization and typically includes contributions from exchange field, demagnetization, anisotropy, and applied field. [8]

The first term causes the magnetization to precess around the effective field, which is also the equilibrium direction of magnetization in the steady state ($d\mathbf{M}/dt = 0$). The second term is the phenomenological Gilbert damping term that represents dissipation in the system and tends to decrease the amplitude of precession and realign the magnetization with the equilibrium direction.

2.3   Spin Transfer Torque

Besides manipulation by magnetic field, the free layer of the MTJ can be manipulated by injection of electric current. In 1996, Slonczewski [2] and Berger [3] independently predicted the effect known as spin transfer torque (STT), also referred to as spin torque (ST). The origin of the effect comes from mutual exchange of angular momentum between the local magnetization and the polarization of electron spins in the current. A ferromagnet acts as a spin filter at its interface, absorbing the transverse components of spin angular momentum and leaving a spin-polarized current exiting the ferromagnet. The spin-polarized current is polarized collinear to the ferromagnet, and when this current is injected into another spin filter (another ferromagnet), the same spin filtering effect occurs (see Fig. 2.4). The components of the polarization transverse to the magnetization of the second ferromagnet are absorbed and apply a torque to the magnetization, which is the spin transfer torque.
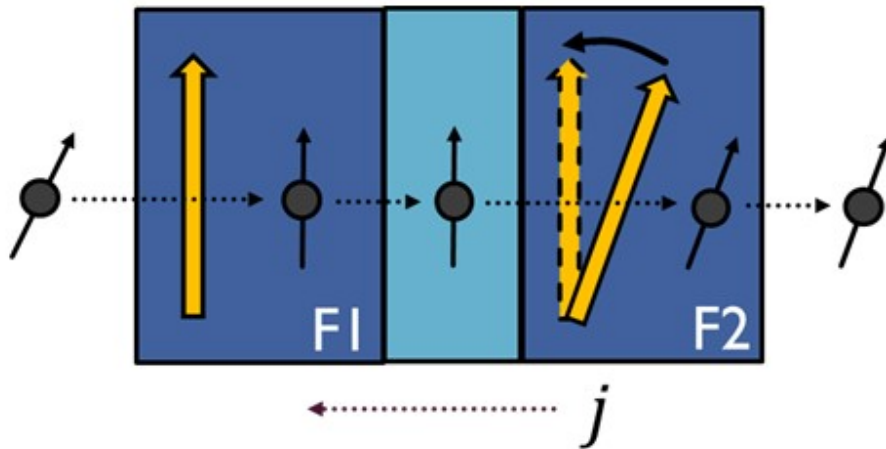
Figure 2.4: **Spin transfer torque.** Spin filtering at the interfaces of ferromagnets leads to spin-polarized currents and the spin transfer torque effect. j is the direction of conventional current, and the circles traveling through the layers represent electron current.

Therefore, the spin-polarized current would apply a torque to the magnetization of the second ferromagnet if the spin polarization of the current and the magnetization are non-collinear.

The torque tends to mutually align the polarization of the current and the magnetization, as shown in Fig. 2.4 and Fig. 2.5.
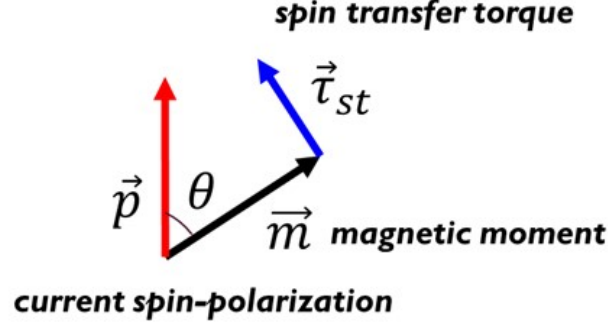

Figure 2.5: **Direction of spin transfer torque.** The spin transfer torque acts to either align or turn away the magnetization from its direction of spin polarization. The torque is proportional to the current and therefore changes sign on reversal of the current polarity.

Magnetization dynamics in the presence of spin torque can be described by the addition of a spin torque term to the LLG equation. The new equation is known as the Landau-Lifshitz-Gilbert-Slonczewski (LLGS) equation, which has the form:

$$\frac{\mathrm{d}\mathbf{M}}{\mathrm{d}t} = -\gamma\mathbf{M} \times \mathbf{H}_{\text{eff}} + \frac{\alpha}{M_s}\mathbf{M} \times \frac{\mathrm{d}\mathbf{M}}{\mathrm{d}t} - \beta(I)g(\theta)\mathbf{M} \times (\mathbf{M} \times \mathbf{p}) \tag{2.7}$$

where $\beta(I)$ is proportional to the current and represents the magnitude of the spin torque, $g(\theta)$ is the angular dependence of the spin torque, and $\mathbf{p}$ is the unit vector describing the spin-polarization of the current. [2, 8] The spin torque term contains a double cross product that captures the geometry of the angular momentum transfer, and the term is proportional to the polarity and amplitude of injected current (see Fig. 2.5).
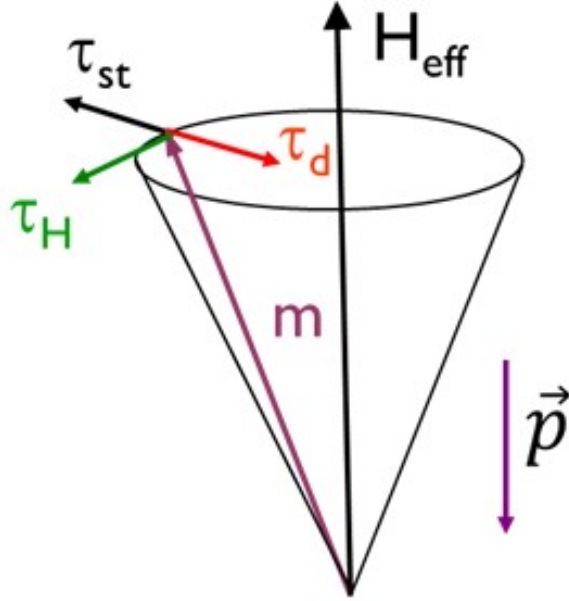
Figure 2.6: **Magnetization dynamics torque diagram.** Schematic of torques for magnetization dynamics involving spin torque. The τ_H is the field and precession torque, the τ_d is the damping torque, and the τ_{ST} is the spin transfer torque. The spin transfer torque can act as anti-damping if the polarization is opposite to the direction of the effective field.

In the appropriate geometry, the spin torque term can act as anti-damping, as shown in Fig. 2.6. This happens when the polarization of the spin current has a component opposite to the direction of effective field. When this is the case, there are three possible regimes of excited magnetization dynamics: damped oscillations, steady-state precession, and switching of the ferromagnet. [2, 8] In the low-current regime, damping still dominates over the effect of spin torque, and the resulting oscillations continue to damp towards the equilibrium direction. In a high current regime, the energy delivered to the system by spin torque cancels the energy lost due to damping and a steady-state precession can occur. At yet higher currents, the spin torque becomes strong enough to overcome the anisotropy energies and reverses direction of the magnetization.

2.4 Voltage-Controlled Magnetic Anisotropy

In addition to spin torque, there has been great interest in manipulation of magnetization by electric field, which relies on the magneto-electric (ME) effect in magnetic solids [17]. One prominent manifestation of the ME effect is modification of magnetic anisotropy in response to applied electric field [23, 24, 25]. A recently discovered ME effect at the interface between a ferromagnetic metal (e.g. Fe) and a non-magnetic insulator (e.g. MgO) [25, 26, 27, 28] is promising for ultra-fast manipulation of magnetization in nanoscale spintronic devices [13]. This interfacial ME effect called voltage-controlled magnetic anisotropy (VCMA) originates from different rates of filling of d-like electron bands at the Fe/MgO interface in response to electric field applied perpendicular to the interface. Since electrons in different bands contribute unequally to the uniaxial perpendicular magnetic anisotropy (PMA) at the Fe/MgO interface, electric field modulates PMA [27, 28]. This electric field induced anisotropy is promising for energy-efficient manipulation of magnetization because, unlike spin torque, it does not rely on high electric current density resulting in large Ohmic losses [29].

VCMA appears in the LLG as an anisotropy term in the effective field. One can write the first-order uniaxial anisotropy energy density as:

$$\varepsilon = K_{u1}\sin^2(\theta) = K_{u1}(1 - (\mathbf{m} \cdot \mathbf{u})^2). \tag{2.8}$$

Here, K_{u1} is the uniaxial anisotropy constant, $\mathbf{m} = \mathbf{M}/M_s$ is the normalized magnetization, and the unit vector $\mathbf{u}$ is along the symmetry axis of the uniaxial anistropy. The VCMA effective field is then:

$$\mathbf{H}_{\text{VCMA}} = -\frac{1}{M_s}\frac{\partial\varepsilon}{\partial\mathbf{m}} = \frac{2K_{u1}}{Ms}(\mathbf{m} \cdot \mathbf{u})\mathbf{u}. \tag{2.9}$$

This leaves the torque due to VCMA as:

$$\tau_{VCMA} = -\gamma \mathbf{M} \times \mathbf{H}_{\text{VCMA}} \propto \frac{2K_{u1}}{Ms} \cos(\theta)\sin(\theta). \tag{2.10}$$

The torque is then maximized when the angle between magnetization and the uniaxial anisotropy axis is at 45 degrees. In the experiment described later, it is not the direct VCMA torque that plays a role in exciting magnetization dynamics but the modulation of the uniaxial anisotropy energy.

2.5 Spin Torque Ferromagnetic Resonance (ST-FMR)

One major application of spin torque to nanomagnetic systems is the spin torque ferromagnetic resonance (ST-FMR) technique. A diagram of the typical circuit for this type of measurement is shown in Fig. 2.7. It consists of a microwave generator, a bias tee, a lock-in amplifier, and optionally a dc bias source of some type (current or voltage). In this technique, an amplitude-modulated microwave current is sent through the ac arm of the bias tee to the device under test and excites magnetization dynamics. Due to the presence of magnetoresistance effects, magnetic oscillations result in oscillations of the device resistance. The ac resistance oscillations then mix with the ac microwave current to produce a dc rectified voltage. The lock-in amplifier detects the voltage by locking in to the modulation frequency of the microwave drive. [30, 31]
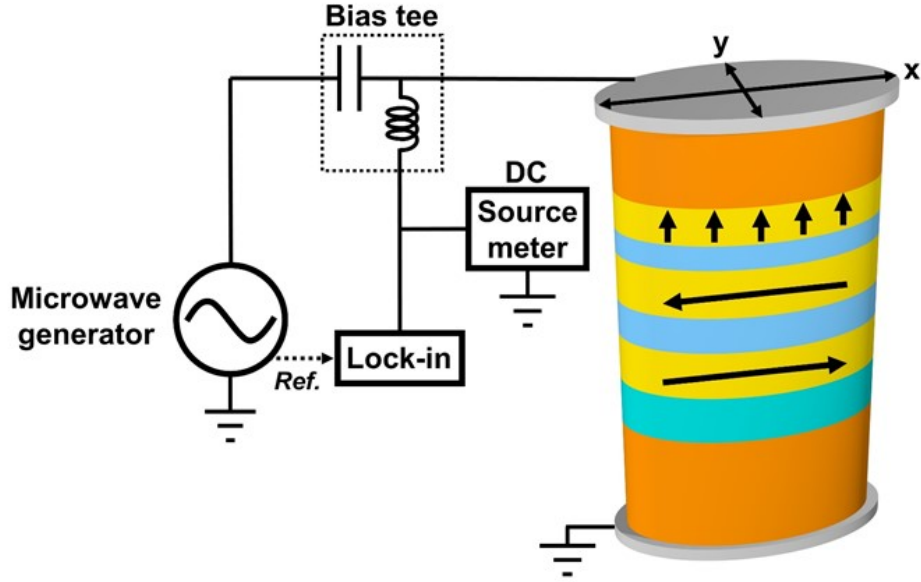
Figure 2.7: **Spin torque ferromagnetic resonance.** Schematic of a spin torque ferromagnetic resonance setup. An amplitude-modulated microwave current is sent through the bias tee to the device and excites magnetization dynamics. The resistance oscillations due to these dynamics mixes with the microwave current to produce a rectified voltage that is detected by lock-in technique.

Typically, one sweeps the microwave drive frequency while holding a constant external magnetic field. When the drive frequency matches that of a magnetic resonance (a spin wave eigenmode), the rectified voltage shows a peak. By changing the applied field, one can record the resonance frequency and field to fit for anisotropy values using the appropriate Kittel formula. One can also fit the linewidth as a function of resonance frequency to obtain a measure of the Gilbert damping of the system. [4] In contrast, conventional ferromagnetic resonance measurements do a field sweep while holding a constant drive frequency. This is also possible in the ST-FMR setup, and it often results in spectra that are easier to interpret if one is interested in fitting the linewidth for damping.

The lineshapes one can see in the ST-FMR spectra have also been thoroughly studied [32, 31]. The curves can generally be well-fitted to symmetric Lorentzian and anti-symmetric Lorentzian line shapes. The different types of torques have also been associated with different

13

lineshapes. The Slonczewski or in-plane spin torque shows up as a symmetric Lorentzian. There is also the field-like spin torque which results in anti-symmetric Lorentzians. [32] The torque due to VCMA also appears as an anti-symmetric Lorentzian in ST-FMR spectra. [15]

2.6 Parametric Excitation

Parametric excitation of magnetic systems is analogous to parametric excitation in classical systems. One prominent example is that of a child on a swing, changing her moment of inertia by moving her legs back and forth in a periodic fashion. The child is modulating a parameter of the system, in this case the moment of inertia of the swing-child pendulum (and thus the resonance frequency), and will excite large-amplitude oscillations at the proper frequency of modulation. This is parametric resonance, and it occurs when a parameter of the system such as the resonance frequency or the damping is modulated at nearly twice the natural frequency of the system.

Parametric excitation of magnetization by external magnetic field has been thoroughly studied in bulk and thin-film ferromagnets [4]. In these experiments, a parameter of the magnetic system (external field) is modulated with a frequency near twice the ferromagnetic resonance frequency f_0 of the system. Parametric excitation is a nonlinear process, in which the parametric drive acts as negative effective magnetic damping competing with positive intrinsic damping [4, 5]. At a threshold amplitude of the parametric drive, the negative damping exceeds the intrinsic damping and magnetization oscillations with a frequency near f_0 are excited.

Parametric excitation of magnetization has several important advantages over direct excitation by external magnetic field with a frequency near f_0. First, parametric excitation efficiently couples not only to the uniform precession of magnetization but also to other spin

wave eigenmodes. This allows excitation of short wavelength spin waves by simply choosing the parametric drive frequency to be twice the desired spin wave frequency. Second, parametric pumping can be used for frequency-selective amplification of spin waves [22]. Third, it can be employed for spin wave amplification and phase error corrections [18]. All these properties of parametric pumping are highly desirable for manipulation of magnetization in the field of nanomagnonics [19, 20]. However, parametric excitation of spin waves by microwave magnetic field in metallic ferromagnets is not energy efficient because of the relatively high threshold fields (tens of Oe) [21] and the relatively high currents needed to generate them. Replacing magnetic field pumping by electric field (VCMA) pumping solves this problem and allows parametric excitation of magnetic oscillations in metallic ferromagnets by a low-power microwave drive.

Chapter 3

Parametric Resonance Excited by Electric Field

Here I show that magnetic oscillations in a nanoscale magnetic tunnel junction can be generated via electric field induced parametric resonance. In the experiment, microwave electric field at twice the ferromagnetic resonance frequency modulates perpendicular magnetic anisotropy of the MTJ free layer and thereby parametrically excites oscillations of its magnetization.

3.1   Device and DC Characterization

The devices under study are elliptical nanoscale magnetic tunnel junctions with lateral dimensions 70 nm×150 nm, schematically shown in Fig. 3.1. The junctions are patterned from (bottom lead)/ Ta(5)/ PtMn(15)/ SAF/ MgO(0.83)/ $Co_{20}Fe_{60}B_{20}(1.58)$/ Ta(5)/ (cap) multilayers (thicknesses in nm) deposited by magnetron sputtering. Here SAF = $Co_{70}Fe_{30}(2.3)$/ Ru(0.85)/ $Co_{40}Fe_{40}B_{20}(2.4)$ is the pinned synthetic antiferromagnet, which has magnetic

moments lying in the plane of the sample. The equilibrium direction of the $Co_{20}Fe_{60}B_{20}$ free layer magnetization is normal to the sample plane due to interfacial PMA [15]. Prior to patterning, the multilayers are annealed for 2 hours at 300 °C in a 10 kOe in-plane magnetic field that sets the pinned layer exchange bias direction parallel to the MTJ long axis.
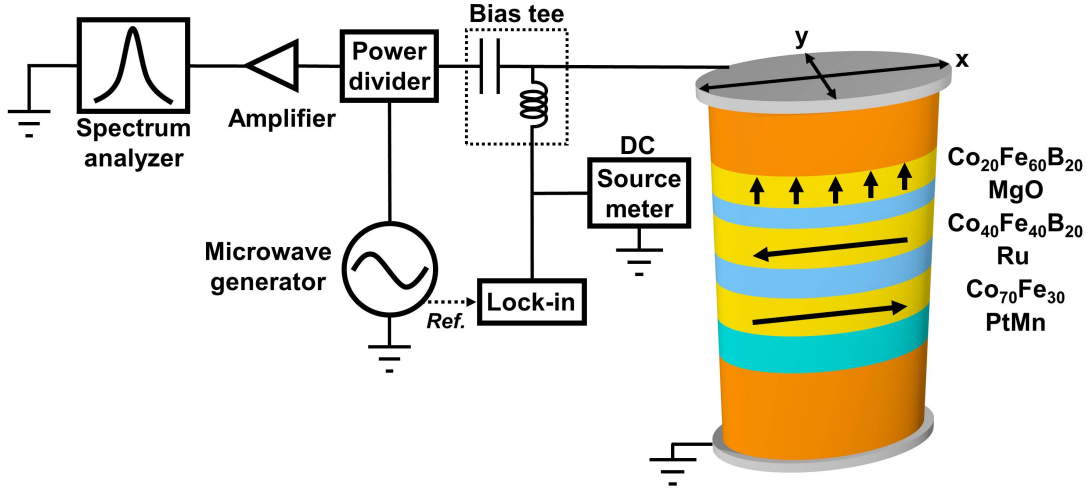

Figure 3.1: **Measurement setup for electrical characterization.** Schematic of the measurement setup.

All measurements were made in the setup schematically shown in Fig. 3.1. The setup has a microwave generator, a spectrum analyzer, a microwave amplifier, and a DC sourcemeter connected through a bias tee and power divider. The circuit is connected to the sample by a microwave probe. This setup allows application of DC and microwave voltages to the MTJ, and it also allows measurement of DC and microwave signals generated by the MTJ.

First, a DC measurement is made to characterize the device resistance, which will be important for figuring out the magnetic state and calculating the amplitude of microwave drive. Fig. 3.2 shows conductance G of the MTJ measured as a function of in-plane magnetic field H_x applied parallel to the MTJ long axis. The shape of the $G(H_x)$ curve is congruent to the shape of the $M_x(H_x)$ hysteresis loop [15], where M_x is the normalized projection of the free layer magnetization onto the applied field direction. The hysteresis loop confirms the

out-of-plane easy axis of the free layer. The center of the loop is shifted from zero field due to a residual 0.06 kOe stray field from the SAF.
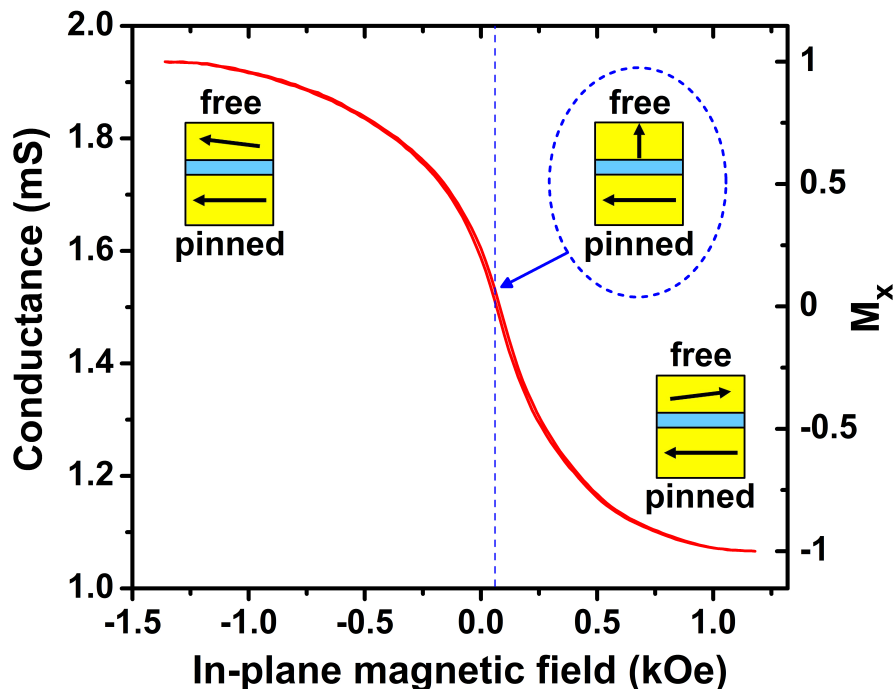

Figure 3.2: **MTJ conductance and magnetic configuration.** MTJ conductance as a function of in-plane magnetic field H_x applied parallel to the MTJ long axis. The diagrams indicate the magnetic configuration at different parts of the conductance curve.

3.2 Spin Torque Ferromagnetic Resonance

Prior to performing microwave measurements, the circuit without the sample was calibrated so the microwave generator would source flat power as a function of excitation frequency. Since the parametric excitation amplitude is a function of microwave drive frequency and amplitude, this calibration is key to ensuring consistent measurement of the threshold required for parametric resonance. The calibration was done by placing a power meter in place of the sample location and sourcing microwave signal from the generator while the amplifier was powered on. Power flatness was calibrated to within less than $0.1\,\mathrm{dB}$ of the setpoint

power, as delivered to a $50\,\Omega$ load. Impedance mismatch between the microwave equipment and the MTJ will change the microwave current and voltage at the sample, which is taken into account through characterization of the MTJ resistance as mentioned above. In principle, imaginary parts of the impedance could come into play through parasitic capacitances or inductances, but this was not taken into account in this experiment and is thus assumed to be negligible. [7]

We employ spin torque ferromagnetic resonance to characterize the spectral properties of the spin wave eigenmodes of the MTJ. I will briefly review the technique and introduce notation that is used later in describing the parametric resonance signal. As mentioned previously, a small amplitude microwave drive current $GV_{\text{ac}}\sin(2\pi f_{\text{d}}t)$ is applied to the MTJ and excites oscillations of magnetization at the drive frequency f_{d}. Here, G is the device conductance, V_{ac} is the amplitude of the microwave voltage, and f_{d} is the drive frequency. The resulting resistance oscillations $R_{\text{ac}}\sin(2\pi f_{\text{d}}t + \phi)$ of the MTJ at the drive frequency lead to partial rectification of the microwave drive voltage V_{ac} and generate a direct voltage V_{r}. Here, R_{ac} is the amplitude of the ac resistance oscillations and ϕ is the phase difference between resistance oscillations and microwave drive, which can be different from zero. Peaks (or dips) in ST-FMR spectra $V_{\text{r}}(f_{\text{d}})$ arise from resonant excitation of spin wave eigenmodes of the MTJ [30, 31].
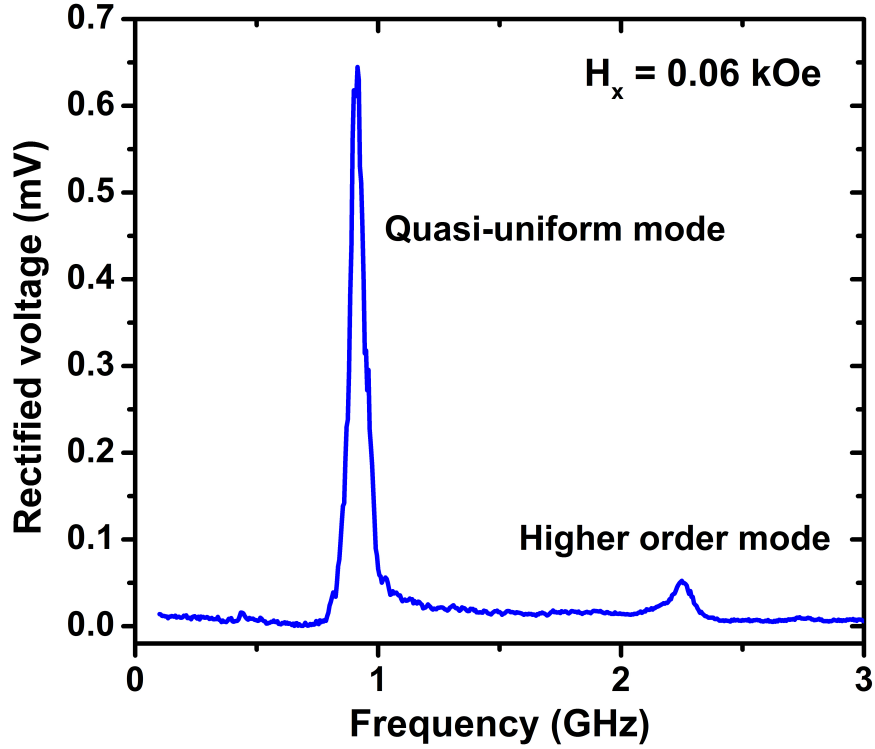
Figure 3.3: **ST-FMR spectrum.** ST-FMR spectrum measured at $H_x = 0.06$ kOe.

Fig. 3.3 shows an ST-FMR spectrum of the MTJ measured at $H_x = 0.06$ kOe. Two spin wave eigenmodes are present in this spectrum with the lowest-frequency ($f_0 = 0.91$ GHz) mode being the quasi-uniform mode of the free layer [34]. From the spectral linewidth of the quasi-uniform mode we can estimate the Gilbert damping parameter to be $\alpha \sim 0.0384$, which is typical for a CoFeB layer of this thickness [15]. Dependence of ST-FMR spectra on H_x is summarized in Fig. 3.4. The frequency of the quasi-uniform mode increases with increasing absolute value of the net in-plane field due to the second order uniaxial PMA present in this system [15].
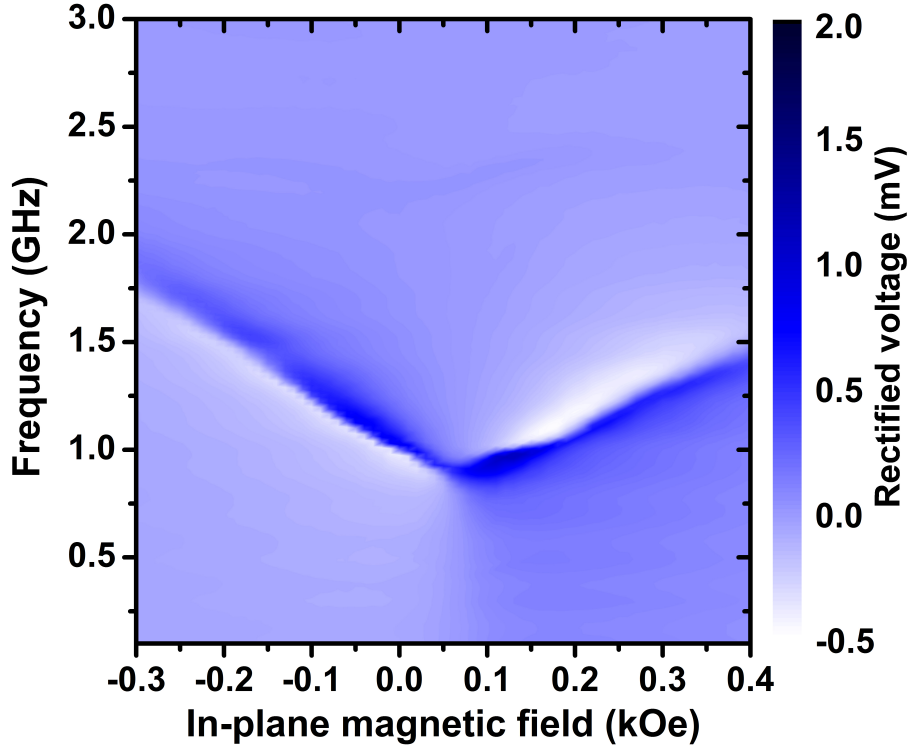
Figure 3.4: **ST-FMR f(H) contour plot.** Dependence of ST-FMR spectra on H_x.

Fig. 3.5 shows dependence of the quasi-uniform mode frequency on direct voltage bias V_{dc} applied to the MTJ. The observed linear frequency shift arises exclusively from VCMA because Ohmic heating, damping-like ST, and field-like ST are all expected to induce quadratic frequency shifts in V_{dc} for the perpendicular orientation of the SAF and free MTJ layers employed in this experiment. The slope of the line in Fig. 3.5 is approximately equal to $(\gamma/2\pi)(dH_u/dV_{dc})$, where the gyromagnetic ratio γ is taken to be $176\,\text{GHz/T}$ and H_u is the PMA effective field. The data in Fig. 3.5 gives VCMA efficiency $dH_u/dV_{dc} = 526\,\text{Oe/V}$, which is typical for this material system [15].
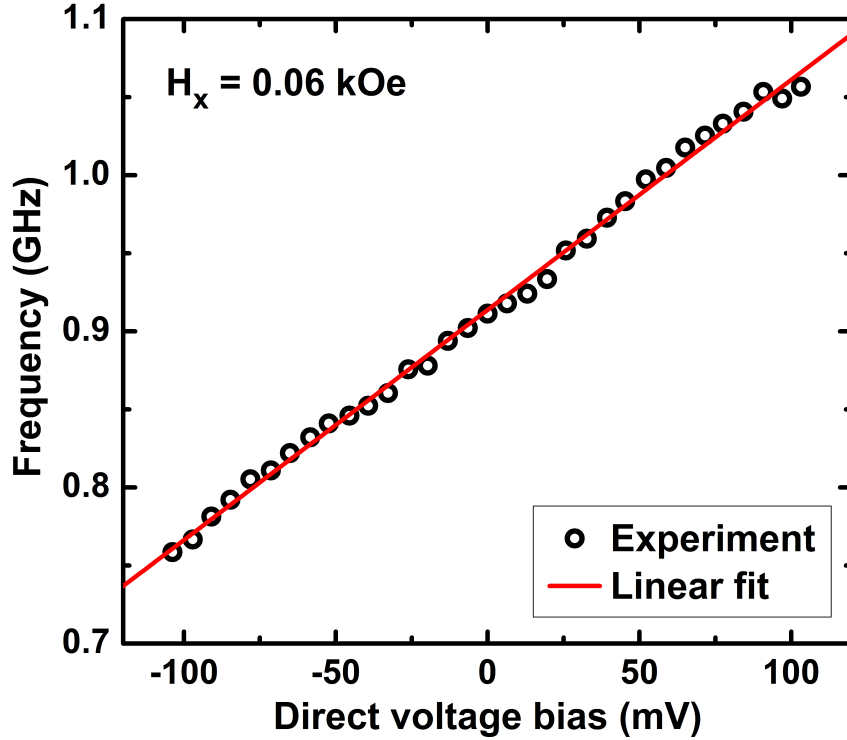
Figure 3.5: **Quasi-uniform mode frequency vs. voltage.** Quasi-uniform mode frequency versus direct voltage bias V_{dc} measured at $H_x = 0.06$ kOe.

3.3 Microwave Emission Measurements

After we have characterized the possible excitation modes via ST-FMR, we can attempt to excite these modes parametrically (through vCMA) rather than by direct excitation (through ST). We use the so-called parallel pumping geometry to parametrically excite the free layer quasi-uniform mode [16]. In this geometry, magnetization of the free layer is parallel to the oscillating PMA effective field H_u. We apply a constant 0.06 kOe in-plane magnetic field along the long axis of the ellipse to compensate the in-plane SAF stray field acting on the free layer. We then apply a parametric drive voltage V_{ac} to the MTJ at drive frequency f_d near $2f_0$ (twice the resonance frequency of the quasi-uniform mode). The microwave voltage results in modulation of PMA at the drive frequency, f_d, due to VCMA. This can

parametrically excite magnetization oscillations at half the drive frequency, $f_d/2$, [16] which gives rise to the MTJ resistance oscillations

$$R_{ac} \cos(2\pi \frac{f_d}{2} t + \phi).$$ (3.1)

These resistance oscillations can be detected via their mixing with the microwave current

$$GV_{ac} \cos(2\pi f_d t)$$ (3.2)

through the junction, which generates voltage signals proportional to R_{ac} at frequencies $f_d/2$ and $3f_d/2$:

$$\begin{aligned}
V_{mix}(t) &= GV_{ac} \cos(2\pi f_d t) \cdot R_{ac} \cos\left(2\pi \frac{f_d}{2} t + \phi\right) \\
&= \frac{1}{2} GV_{ac} R_{ac} \left[\cos\left(2\pi \frac{f_d}{2} t - \phi\right) + \cos\left(2\pi \frac{3f_d}{2} t + \phi\right)\right].
\end{aligned}$$ (3.3)

Therefore, in order to detect the parametric resonance, we tune the spectrum analyzer to a window around the ferromagnetic resonance frequency f_0. As we sweep through the microwave drive frequencies near twice the resonance frequency $2f_0$, we should detect emissions on the spectrum analyzer if we do indeed excite parametric resonance.

As illustrated in Fig. 3.1, we amplify $V_{mix}(t)$ and measure its spectrum with a microwave spectrum analyzer. We used a $+22\,\mathrm{dB}$ gain amplifier which operates in the frequency range $0.1\,\mathrm{GHz}$ to $1.5\,\mathrm{GHz}$, and this gain was accounted for in the later analysis of microwave drive amplitude.

3.4 Experimental Results

In this section, I present power spectra of $V_{\mathrm{mix}}(t)$ measured by the spectrum analyzer near $f_{\mathrm{d}}/2$. Similar spectra are observed near $3f_{\mathrm{d}}/2$. Fig. 3.6 displays power spectral density (PSD) $P(f)$ of $V_{\mathrm{mix}}(t)$ measured at several fixed values of the drive frequency f_{d} near $2f_0$ and drive amplitude $V_{\mathrm{ac}} = 0.185$ V. The maximum of each power spectrum is observed exactly at $f_{\mathrm{d}}/2$, clearly illustrating that magnetization dynamics of the free layer is excited parametrically at half the drive frequency. The linewidths of the measured spectral peaks are in the range of several MHz. This linewidth mostly arises from thermal fluctuations of the free layer magnetization (fluctuations of the phase ϕ and amplitude R_{ac} in equation (3.3)). Fig. 3.7 illustrates that parametric excitation of the quasi-uniform mode has well-pronounced resonant character: significant amplitude of the parametric oscillations is observed only in a narrow range of the drive frequencies near $2f_0$.
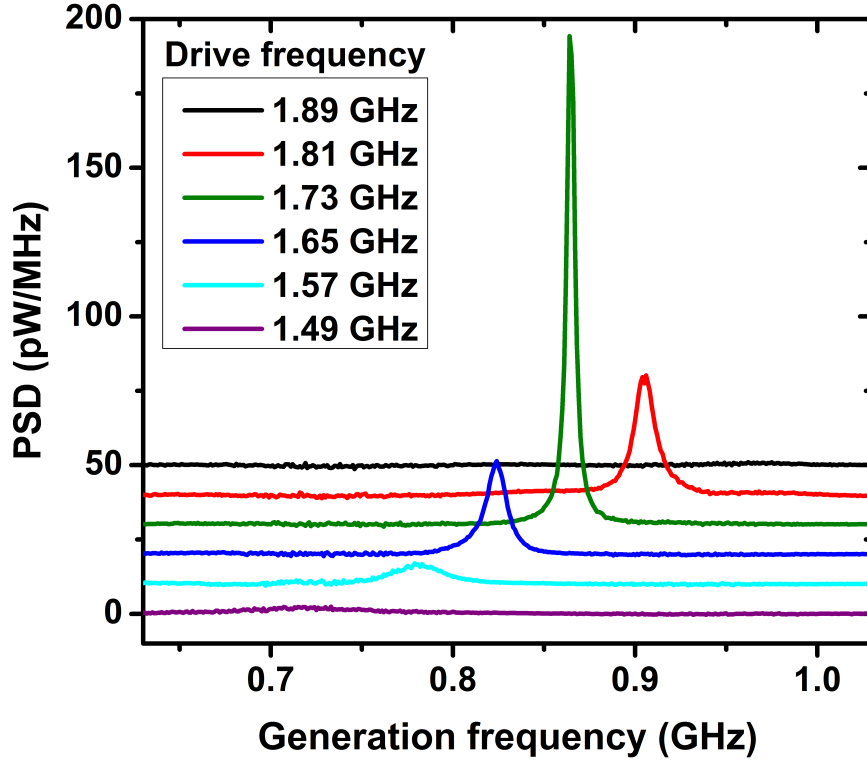
Figure 3.6: **Power spectral density of parametric resonance signal.** Power spectral density (PSD) of the microwave signal emitted by the MTJ under VCMA parametric drive of $V_{ac} = 0.185$ V. Curves are vertically offset for clarity.

Fig. 3.8 displays dependence of $P(f_d/2)$ on the drive amplitude V_{ac} and drive frequency f_d. This figure illustrates the parametric excitation efficiency and clearly demonstrates that the observed microwave emission from the sample shows a threshold character in V_{ac}. This threshold behavior is expected for parametric resonance that is excited when effective negative damping from the parametric drive exceeds the positive natural damping of the excited mode [4, 5]. Fig. 3.8 also shows that the parametric resonance frequency f_{pr} (defined as the drive frequency f_d that gives maximum power $P(f_d/2)$ at a given value of microwave drive V_{ac}) shifts to lower values with increasing drive amplitude, as expected for a uniaxial ferromagnet [11]. The shape of the parametric instability region in Fig. 3.8 is a typical Arnold tongue of a nonlinear parametric oscillator [33].
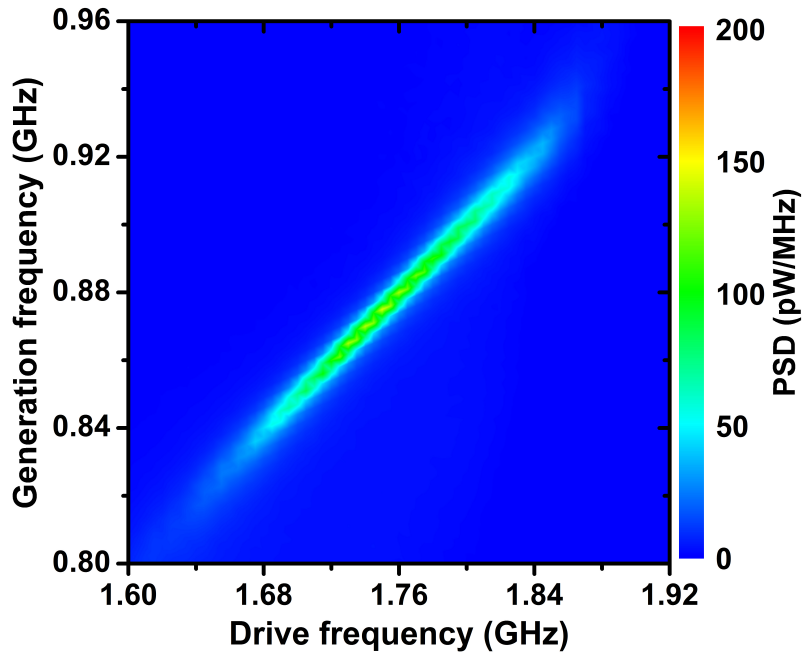
Figure 3.7: **Power spectral density contour plot.** Dependence of the parametrically generated emission spectra on the drive frequency.
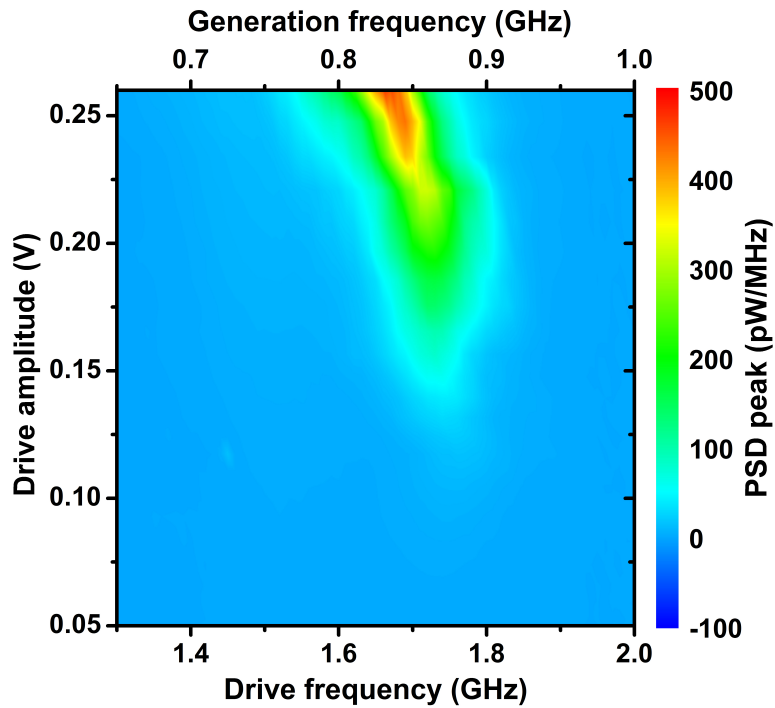

Figure 3.8: **PSD contour vs. frequency and drive amplitude.** PSD peak plotted versus drive frequency and drive amplitude reveals typical Arnold tongue shape characteristic of parametric excitation.

3.5 Theory and Analysis

Here, I describe the theory developed by our collaborators: Roman Verba, Vasil Tiberke-vich, and Andrei Slavin. The theory describes how to calculate the threshold of parametric resonance excited by VCMA in the presence of thermal fluctuations. We used this theory to experimentally determine the threshold in our system. In the theoretical description of the MTJ magnetization dynamics we use the macrospin approximation, assuming uniform magnetization distribution inside the free layer. We use an expansion of the free layer magnetization into static and dynamic parts: $\mathbf{M}(t) = M_s(\boldsymbol{\mu} + c(t)\mathbf{m} + c^*(t)\mathbf{m}^*)$, where $\boldsymbol{\mu}$ is the unit vector in the direction of the static magnetization, $\mathbf{m}$ is the vector structure of the quasi-uniform spin wave mode, and c is the dimensionless amplitude of the quasi-uniform spin wave mode. One can derive the following dynamic equation [4, 16]:

$$\frac{\mathrm{d}c}{\mathrm{d}t} + i(\omega_0 + T|c|^2)c + \Gamma c = h_{\mathrm{p}} V_{00} e^{i\omega_p t} c^* + \eta(t) \tag{3.4}$$

where $\omega_0 = 2\pi f_0$ is the ferromagnetic resonance (angular) frequency, T is the nonlinear frequency shift, and Γ is the damping rate. h_{p} is the effective pumping field, V_{00} is the efficiency of parametric interaction, and the term $\eta(t)$ describes thermal noise (details in [37]).

3.5.1 Theoretical Calculation of the Threshold

The excitation threshold can be theoretically calculated and compared to our experimental value. It is given by [4, 16] $h_{th} = \Gamma/V_{00}$ in units of A/m. The parametric interaction efficiency is equal to [16]:

$$|V_{00}| = \frac{\gamma\mu_0}{2}\varepsilon, \quad \varepsilon = \left|\frac{\mathbf{m}^* \cdot \mathbf{m}^*}{(\mathbf{m}^* \cdot (\boldsymbol{\mu} \times \mathbf{m}))}\right| \tag{3.5}$$

where γ is the gyromagnetic ratio taken to be $176\,\text{GHz/T}$ as before, μ_0 is the permeability of vacuum, and ε is the averaged ellipticity of the quasi-uniform mode. The damping rate $\Gamma = 2\pi \times 0.0351\,\text{GHz}$ we obtained as the half width at half maximum (HWHM) from ST-FMR measurements. Since the mode profile in an out-of-plane magnetized elliptical disk is generally not entirely uniform, the mode ellipticity was calculated using a micromagnetic mode profile using the MuMax3 simulation software [36]. The calculation gives $\varepsilon \sim 0.26$ and results in a threshold value of $h_{\text{th}} = 89\,\text{Oe}$, or $V_{\text{th}} = 0.169\,\text{V}$ by using the experimental VCMA efficiency.

If one were to use the uniform mode approximation, $\varepsilon = \omega_M |N_x - N_y|/(2\omega_0)$, where $\omega_M = 2\pi M_s$ (with $M_s = 950{,}000\,\text{A/m}$), N_x and N_y are the components of the demagnetization tensor, and $\omega_0 = 2\pi \times 0.9113\,\text{GHz}$ is the resonance frequency. For our elliptical nanopillar geometry, we use the theory of [38] to calculate $N_x = 0.014$ and $N_y = 0.040$. In this case, the ellipticity is much higher $\varepsilon = 0.477$, and the threshold is found to be $h_{\text{th}} = 52.5\,\text{Oe}$, or $V_{\text{th}} = 0.100\,\text{V}$.

3.5.2   Experimental Determination of the Threshold

In experiment, the exact position of the excitation threshold could be determined by fitting the dependence of oscillation power on microwave drive amplitude.

Data Analysis

In order to quantitatively determine the experimental value of the threshold drive voltage V_{th} needed to excite parametric resonance of the quasi-uniform mode, we analyze reduced power of this mode p as a function of the drive amplitude V_{ac}. By definition, $p = |c|^2$ where c is the dimensionless amplitude of the quasi-uniform mode as described previously. c is

proportional to the amplitude of the MTJ resistance oscillations, so that $p \sim (GR_{ac})^2$. It is clear from equation (3.3) that PSD of the reduced power $p(f)$ is proportional to $P(f)/V_{ac}^2$ for any V_{ac}. In Fig. 3.9a, we plot its resonant value $P(f_{pr}/2)/V_{ac}^2$, which is proportional to $p(f_{pr}/2)$, as a function of V_{ac}.
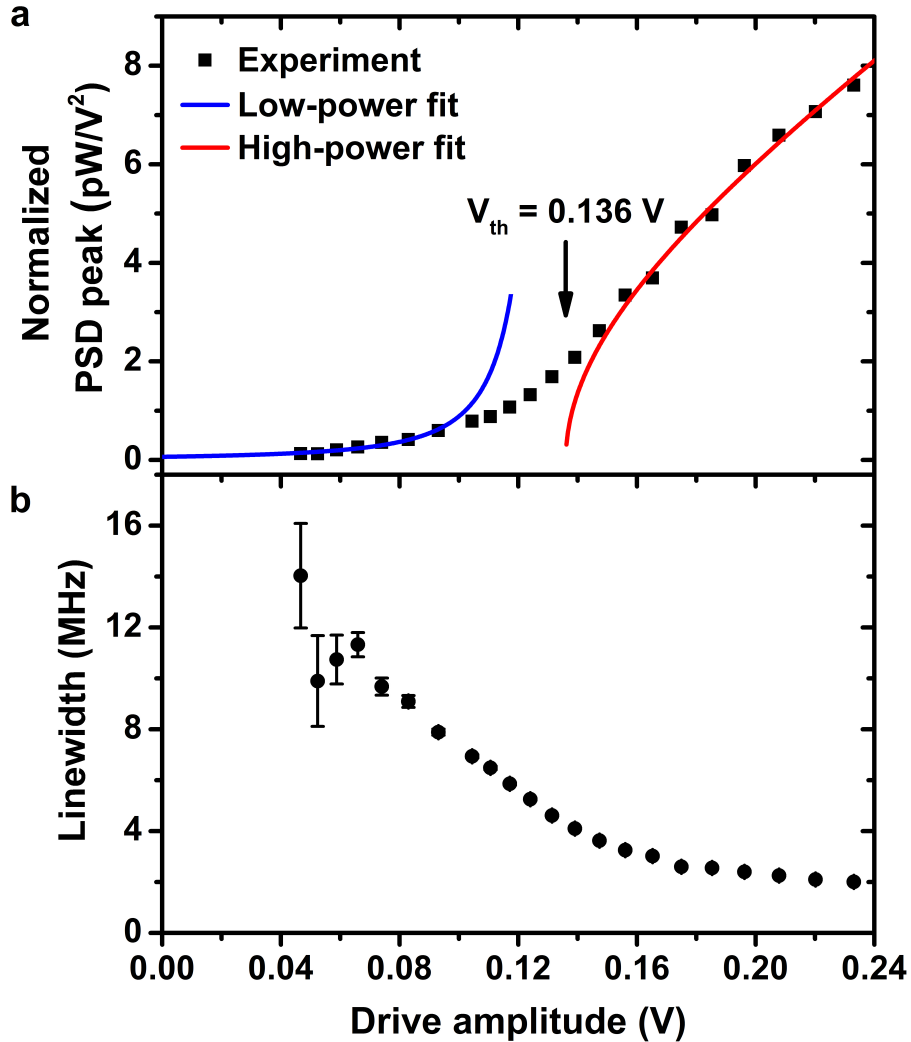
Figure 3.9: **Parametric resonance threshold.** **a**, Normalized PSD peak amplitude $P(f_{pr}/2)/V_{ac}^2$ measured at parametric resonance as a function of the parametric drive amplitude V_{ac}. Best fits of equation (3.6) and equation (3.7) to the data (solid lines) give the parametric resonance threshold voltage $V_{th} = 0.136$ V. **b**, Dependence of the PSD spectral linewidth (half width at half maximum) on the parametric drive amplitude V_{ac} measured at parametric resonance.

Analytic expressions for $p(f_{pr}/2)$ have been derived in the limit of $V_{ac} \ll V_{th}$. In this limit, magnetization dynamics are small-amplitude thermal fluctuations amplified by the parametric drive:

$$p(f_{pr}/2) = \frac{C_1}{(V_{th} - V_{ac})^2}. \tag{3.6}$$

In the opposite limit of $V_{ac} \gg V_{th}$, thermal fluctuations can be neglected and the following analytic expression for the reduced power p can be derived:

$$p = C_2\sqrt{V_{ac}^2 - V_{th}^2}. \tag{3.7}$$

For our system, p in equation (3.7) can be replaced by $p(f_{pr}/2)$ because the measured spectral linewidth of $P(f)$ at $f_d = f_{pr}$ shown in Fig. 3.9b depends weakly on V_{ac} for $V_{ac} > 0.16$ V. Therefore, we can fit the data in Fig. 3.9a using equation (3.6) in the small amplitude limit and equation (3.7) in the large amplitude limit. The best fit to the data in the $V_{ac} \ll V_{th}$ ($V_{ac} \gg V_{th}$) limit shown by the blue (red) line in Fig. 3.9a gives $V_{th} = 0.136$ V. In this fitting procedure, C_1 and C_2 are free fitting parameters while V_{th} is treated as a common fitting parameter for both the small and large amplitude limits. (See the next section on fitting.)

It is instructive to compare the measured V_{th} to its theoretically expected value, which was calculated for the MTJ geometry and the measured VCMA efficiency. The calculated threshold voltage for the case of a uniform mode was $V_{th} = 0.100$ V while using a non-uniform mode profile from simulations yielded $V_{th} = 0.169$ V. The experimental value is between these two values, which lends support to the VCMA origin of the observed parametric resonance. This indicates the experimentally excited mode is not entirely uniform, and the mode profile found in simulation might not match the one in experiment. We could reasonably attribute

the discrepancy to deviation of the sample shape from the ideal elliptical cylinder shape, which would have a large impact on the ellipticity of the excited mode.

In our experiment, spin-polarized tunneling current flows through the MTJ, which results in ST and Oersted field acting on the free layer. However, these types of drive play a negligible role in exciting parametric resonance compared to the VCMA drive. The Oersted field has nearly circular symmetry and therefore it poorly couples to the quasi-uniform mode. The field-like ST was shown to be small compared to the damping-like ST in previous studies of these samples [15]. The effective field of the damping-like ST lies in the sample plane, which corresponds to perpendicular pumping geometry. It is known that parametric excitation of the quasi-uniform mode is not possible in this geometry.

Fitting

The fitting was done with Python by using the `leastsq` method in the `scipy.optimize` module. The function performs a least-squares method of non-linear curve fitting. In this particular case, the two fitting functions were applied to different regions of the normalized peak power as a function of drive voltage, which is proportional to the reduced power $p(V_{\mathrm{ac}})$. The threshold V_{th} was the common parameter between fitting functions. The errors (differences between fit and data) were calculated individually for each fitting region, and then these errors were concatenated as the total error to be reduced by the `leastsq` function, eventually converging on the threshold $V_{\mathrm{th}} = 0.136\,\mathrm{V}$.

We chose the data range where $V_{ac} < 0.1$ V for the low-power fit because at that point the threshold does not change significantly (less than ∼0.1% relative error) if a lower cutoff is selected. If one chooses to include one more data point to the right, the threshold changes by ∼1%.

We chose the data range where $V_{ac} > 0.16$ V for the high-power fit because it is the region when linewidth does not vary much so we can neglect thermal effects and use the analytic function derived for high drive amplitude.

3.6 Parametric Resonance Detected by ST-FMR

Our experiment employs an MTJ magnetic configuration with in-plane SAF and out-of-plane free layer. It is convenient for unambiguous demonstration and quantitative analysis of parametric resonance excited by VCMA. However, we find that VCMA-driven parametric resonance is ubiquitous and can be observed in other types of MTJ configurations as well. Fig. 3.10 shows the out-of-plane magnetic field dependence of ST-FMR spectra measured for a 30 nm×95 nm MTJ with out-of-plane equilibrium configuration of both the free and SAF layers. Because of the smaller amplitude of the ST-FMR rectified voltage in this collinear geometry, we employed ultra-sensitive ST-FMR with magnetic field modulation [34] rather than conventional ST-FMR with amplitude modulation.
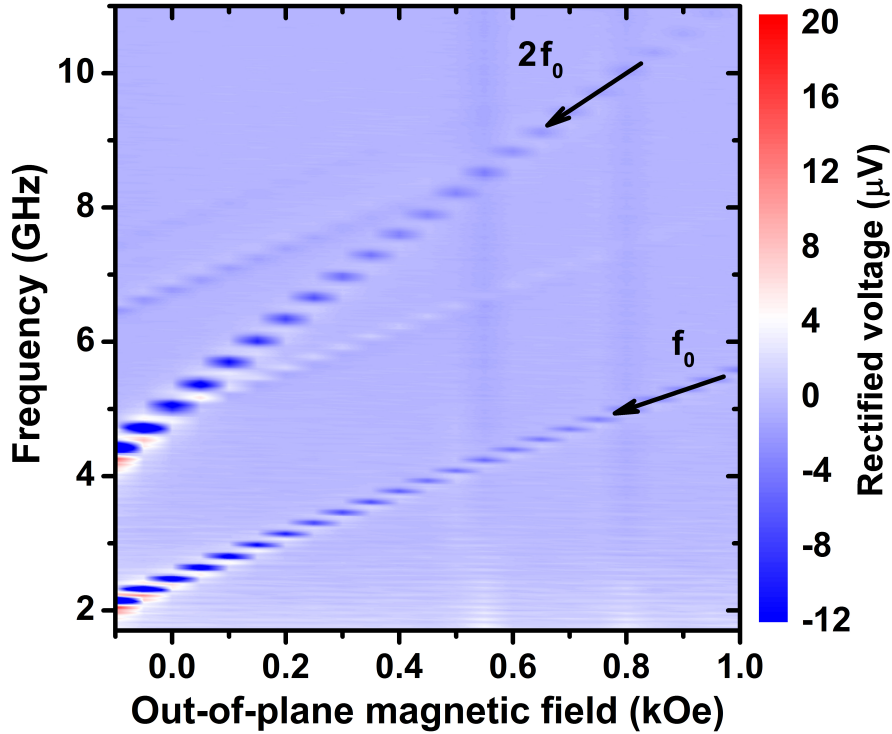
Figure 3.10: **Parametric resonance in ST-FMR.** ST-FMR spectra of an MTJ with out-of-plane SAF and free layers measured as a function of out-of-plane magnetic field. Resonance at twice the quasi-uniform mode frequency arises from parametric excitation of the quasi-uniform mode.

The ST-FMR spectra measured at a large value of the microwave drive voltage $V_{ac} = 0.396$ V reveal several spin wave eigenmodes of the free layer. Another prominent resonance is observed at twice the frequency of the lowest-frequency (quasi-uniform) spin wave eigenmode. In this collinear MTJ geometry, the microwave resistance oscillations of the device have a significant component at twice the excited spin wave mode frequency and mix with the parametric drive at twice the mode frequency to give rise to a rectified voltage peak at $2f_0$ measured by ST-FMR. The amplitude of this additional resonance at $2f_0$ relative to the amplitude of the resonance at f_0 increases with increasing V_{ac}, which is a signature of a thermally smeared threshold behavior similar to that in Fig. 3.9a. The out-of-plane collinear geometry is commonly employed in spin transfer torque magnetic random access memory

(STT-MRAM), and parametric resonance signals in ST-FMR of STT-MRAM can potentially be used for characterization of the free layer properties such as magnetic damping.

Chapter 4

Conclusion

In summary, this work shows that magneto-electric coupling can be used to excite parametric resonance of magnetization by electric field. We employed voltage-controlled magnetic anisotropy at the CoFeB/MgO interface to excite parametric oscillations of a CoFeB free layer magnetization in nanoscale magnetic tunnel junctions. The threshold voltage for parametric excitation in this system is found to be well below 1 Volt, which is attractive for applications in energy-efficient spintronic and magnonic nanodevices such as spin wave logic [35]. This work opens a new route for excitation of magnetization dynamics in thin films of metallic ferromagnets and nanodevices based on magnetic multilayers.

For future work, parametric excitation of magnetization is a versatile method for generating short-wavelength spin waves [16]. A natural extension of this work is to develop nanowire devices based on those proposed in [16], using ferromagnetic metals in a nanowire geometry with contacts that utilize VCMA to generate and manipulate propagating spin waves.

Bibliography

[1] Slonczewski, J. C. Conductance and exchange coupling of two ferromagnets separated by a tunneling barrier. *Phys. Rev. B* **39**, 6995 (1989).

[2] Slonczewski, J. C. Current-driven excitation of magnetic multilayers. *J. Magn. Magn. Mater.* **159**, L1 (1996).

[3] Berger, L. Emission of spin waves by a magnetic multilayer traversed by a current. *Phys. Rev. B* **54**, 9353 (1996).

[4] Gurevich, A. G., & Melkov, G. A. *Magnetization Oscillations and Waves* (CRC, 1996).

[5] L'vov, V. S. *Wave Turbulence Under Parametric Excitation* (Springer, 1994).

[6] O'Handley, R. C. *Modern Magnetic Materials Principles and Applications* (John Wiley and Sons, 2000).

[7] Pozar, D. M. *Microwave Engineering* (Wiley, 2004).

[8] Ralph, D. and Stiles, M. Spin transfer torques. *J. Magn. Magn. Mater.* **320**, 1190 (2008).

[9] Butler, W. H. *et al.* Spin-dependent tunneling conductance of Fe—Mgo—Fe sandwiches. *Phys. Rev. B* **63** 054416 (2001).

[10] Julliere, M. Tunneling between ferromagnetic films. *Physics Letters A* **54**, 225 (1975).

[11] Kiselev, S. I. *et al.* Microwave oscillations of a nanomagnet driven by a spin-polarized current. *Nature* **425**, 380 (2003).

[12] Matsukura, F., Tokura, Y., & Ohno, H. Control of magnetism by electric fields. *Nature Nanotech.* **10**, 209-220 (2015).

[13] Shiota, Y. *et al.* Induction of coherent magnetization switching in a few atomic layers of FeCo using voltage pulses. *Nature Mater.* **11**, 3943 (2012).

[14] Nozaki, T. *et al.* Electric-field-induced ferromagnetic resonance excitation in an ultrathin ferromagnetic metal layer. *Nature Phys.* **8**, 491496 (2012).

[15] Zhu, J. *et al.* Voltage-induced ferromagnetic resonance in magnetic tunnel junctions. *Phys. Rev. Lett.* **108**, 197203 (2012).

[16] Verba, R., Tiberkevich, V., Krivorotov, I. N. & Slavin, A. Parametric excitation of spin waves by voltage-controlled magnetic anisotropy. *Phys. Rev. Applied* **1**, 044006 (2014).

[17] Fiebig, M. Revival of the magnetoelectric effect. *J. Phys. D* **38**, R123 (2005).

[18] Chumak, A. V. Vasyuchka, V. I., Serga, A. A., Kostylev, M. P., Tiberkevich, V. S., & Hillebrands, B. Storage-recovery phenomenon in magnonic crystal. *Phys. Rev. Lett.* **108**, 257207 (2012).

[19] Kruglyak, V. V., Demokritov, S. O., & Grundler, D. Magnon spintronics. *J. Phys. D* **43**, 264001 (2010).

[20] Chumak, A. V., Vasyuchka, V. I., Serga, A. A., & Hillebrands, B. Magnon spintronics. *Nature Phys.* **11**, 453461 (2015).

[21] Urazhdin, S., Tiberkevich, V., & Slavin, A. N. Parametric excitation of a magnetic nanocontact by a microwave field. *Phys. Rev. Lett.* **105** 237204 (2010).

[22] Melkov, G. A., Yu, V., Kobljanskyj, A. A., Serga, A. S., Tiberkevich, V. S., & Slavin, A. N. Reversal of Momentum Relaxation. *Phys. Rev. Lett.* **86**, 4918 (2001).

[23] Weisheit, M., Fhler, S., Marty, A., Souche, Y., Poinsignon, C., & Givord, D. Electric field-induced modification of magnetism in thin-film ferromagnets. *Science* **315**, 349 (2007).

[24] Chiba, D. *et al.* Magnetization vector manipulation by electric fields. *Nature* **455**, 515518 (2008).

[25] Maruyama, T. *et al.* Large voltage-induced magnetic anisotropy change in a few atomic layers of iron. *Nature Nanotech.* **4**, 158161 (2009).

[26] Endo, M., Kanai, S., Ikeda, S., Matsukura, F., & Ohno, H. Electric-field effects on thickness dependent magnetic anisotropy of sputtered MgO/Co40Fe40B20/Ta structures. *Appl. Phys. Lett.* **96**, 212503 (2010).

[27] Duan, C.-G. *et al.* Surface magnetoelectric effect in ferromagnetic metal films, *Phys. Rev. Lett.* **101**, 137201 (2008).

[28] Niranjan, M. K., Duan, C.-G., Jaswal, S. S., & Tsymbal, E. Y. Electric field effect on magnetization at the Fe/MgO(001) interface. *Appl. Phys. Lett.* **96**, 222504 (2010).

[29] Amiri, P. K. & Wang, K. L. Voltage-controlled magnetic anisotropy in spintronic devices. *SPIN* **02**, 1240002 (2012).

[30] Tulapurkar, A. A. *et al.* Spin-torque diode effect in magnetic tunnel junctions. *Nature* **438**, 339342 (2005).

[31] Sankey, J. C. *et al.* Spin-transfer-driven ferromagnetic resonance of individual nanomagnets. *Phys. Rev. Lett.* **96**, 227601 (2006).

[32] Wang, C. *et al.* Bias and angular dependence of spin-transfer torque in magnetic tunnel junctions. *Phys. Rev. B* **79**, 224416 (2009).

[33] Bortolotti, P. *et al.* Parametric excitation of magnetic vortex gyrations in spin-torque nano-oscillators. *Phys. Rev. B* **88**, 174417 (2013).

[34] Gonçalves, A. M. *et al.* Spin torque ferromagnetic resonance with magnetic field modulation. *Appl. Phys. Lett.* **107**, 172406 (2013).

[35] Khitun, A., Bao, M. & Wang, K. L. Magnonic logic circuits. *J. Phys. D* **43**, 264005 (2010).

[36] Vansteenkiste, A. *et al.* The design and verification of MuMax3. *AIP Adv.* **4**, 107133 (2014).

[37] Verba, R. *et al.* Theory of ground-state switching in an array of magnetic nanodots by application of a short external magnetic field pulse. *Phys. Rev. B* **87**, 134419 (2013).

[38] Beleggia, M. *et al.* Demagnetization factors for elliptic cylinders. *J. Phys. D: Appl. Phys.* **38**, 3333 (2005).